J Mater Sci (2013) 48:1196–1204
DOI 10.1007/s10853-012-6859-3

Composition-dependent structural, optical and electrical properties of $In_xGa_{1-x}N$ ($0.5 \leq x \leq 0.93$) thin films grown by modified activated reactive evaporation

S. R. Meher · A. Subrahmanyam · Mahaveer K. Jain

Received: 16 May 2012 / Accepted: 3 September 2012 / Published online: 19 September 2012

Abstract In this report, we have studied the compositional dependence of structural, optical and electrical properties of polycrystalline $In_xGa_{1-x}N$ thin films grown by modified activated reactive evaporation. The growth was monitored by optical emission spectroscopy. The thickness of the films was in the range ~600–800 nm. The phase, crystallinity and composition of the films were determined by X-ray diffraction, Raman spectroscopy and energy dispersive X-ray analysis. The surface morphology was studied by atomic force microscopy. The band gaps of these films obtained from transmittance and photoluminescence measurements were found to vary from 1.88 to 3.22 eV. All the films show *n*-type conductivity. The carrier concentration was found to be decreasing with increase in gallium incorporation which is in good agreement with the free carrier absorption observed in transmittance spectra.

Introduction

InGaN (IGN) has drawn a great deal of attention among the group-III ternary nitride materials due to its immense applications especially in the field of optoelectronics [1–3]. IGN can be considered as a solid solution of InN and GaN. The direct band gaps of InN and GaN are 0.7 and 3.4 eV, respectively. Hence, IGN thin films are promising materials for photovoltaics applications, as its band gap can be tuned in the entire range of solar spectrum [4]. Similar to its constituents, IGN crystallizes predominantly in the hexagonal wurtzite structure in the entire composition range. The basic properties of IGN materials are mostly evaluated on the basis of its binary constituents: InN and GaN. InN, being difficult to grow high quality epilayers, is the least understood material among the group-III nitride semiconductors. Many of its fundamental properties like band gap, electron effective mass, decomposition temperature and defect levels reported in the literature are highly debatable. Recently, the accurate band gap of MBE-grown epitaxial InN film has been shown to be 0.7 eV from photoluminescence (PL) measurements [5]. But, there are reports which still support the earlier result of 1.9 eV [6, 7]. In the literature, several reasons like Burstein–Moss (B–M) shift [8], Mie resonance [9], stoichiometry [10], oxygen impurity [11], defect levels, polycrystallinity, etc., are cited to explain the discrepancy found in the InN band gap. In contrast, almost all the fundamental properties of GaN are well established. Moreover, the structural, optical and electrical properties of IGN films depend mostly on the alloy composition. Thus, the study of the basic properties of IGN alloy system is very difficult and complex.

It is difficult to grow good crystalline quality IGN films in the whole composition range because of several problems. There exists a solid phase miscibility gap in IGN alloy system due to the difference in the interatomic spacing between its constituents, i.e. InN and GaN [12]. Low indium incorporation has also been observed in these alloy films due to the relatively high vapour pressure of InN compared to GaN [13, 14]. Moreover, due to the difference in the formation enthalpies of GaN and InN, surface segregation of indium is expected at the growth front. IGN films can be grown by several techniques like e-beam plasma technique [15], sputtering [16], pulsed laser deposition [17], metalorganic chemical vapour deposition (MOCVD) [18], molecular beam epitaxy (MBE) [19], hydride vapour phase epitaxy [20], etc. In the present scenario, MOCVD and MBE are considered as the leading growth

S. R. Meher (✉) · A. Subrahmanyam · M. K. Jain
Department of Physics, Indian Institute of Technology Madras, Chennai 600036, India
e-mail: samir@physics.iitm.ac.in

techniques to grow high quality IGN epilayers. But, both these techniques employ high temperatures (>500 °C) which limit the growth of good quality indium-rich IGN films. MBE is not a commercially viable technique due to cost factor and low throughput. Though MOCVD is a commercially viable method, use of hazardous gases and high temperatures limit its applications. In order to have compositional tunability (preferably eliminating toxic reactive environments) and to expand the range of applications, a low temperature growth technique is highly desirable.

Recently, our laboratory has developed a room temperature growth technique known as modified activated reactive evaporation (MARE). By this technique, we have grown structurally good quality InN and GaN thin films [21, 22], InN films on flexible substrates like polyimide and polycarbonate [23] and also reported room temperature growth of IGN films using a mixed source of indium and gallium [24]. It may be pointed out that due to the difference in the vapour pressures of indium and gallium, it is always difficult to control the In/Ga ratio from a single evaporation source. A better control over In/Ga ratio may be achieved in IGN alloy films by employing separate sources [25].

In the present study, IGN films in the entire composition range have been grown by MARE technique employing separate In and Ga sources. The dependence of the structural, optical and electrical properties of these thin films on composition has been reported.

Experimental details

The details of the separate source MARE technique are discussed in Ref. [25]. IGN thin films have been prepared on cleaned borosilicate glass (BSG) substrates by MARE technique using a triangular geometry for the evaporation sources and substrate (Fig. 1). The substrate is placed on the radio-frequency (RF) magnetron cathode. The films are grown at room temperature (without any intentional substrate heating). The In/Ga ratio is controlled by capturing the optical emission spectra (OES) through the optical fibres (fitted to the view-port of the vacuum chamber) using Ocean Optics HR 2000 spectrometer. OES records the characteristic emission lines of the plasma. The emission spectra consist of the excited indium, gallium and nitrogen species (Fig. 2). The thickness of IGN films is in the range 600–800 nm as determined by the reflectance spectra of Filmetrics F20 spectrophotometer. The phase and crystallinity of the IGN films are studied using Phillips X'Pert Pro X-ray diffractometer operated at 40 kV and 30 mA using Cu Kα source ($\lambda = 0.1542$ nm). The Raman spectra are recorded using a Jobin–Yvon HR-800 Raman spectrometer equipped with an 18 mW Ar^+ laser source (488 nm). The energy dispersive X-ray analysis (EDX) is performed using the EDAX detector attached to a

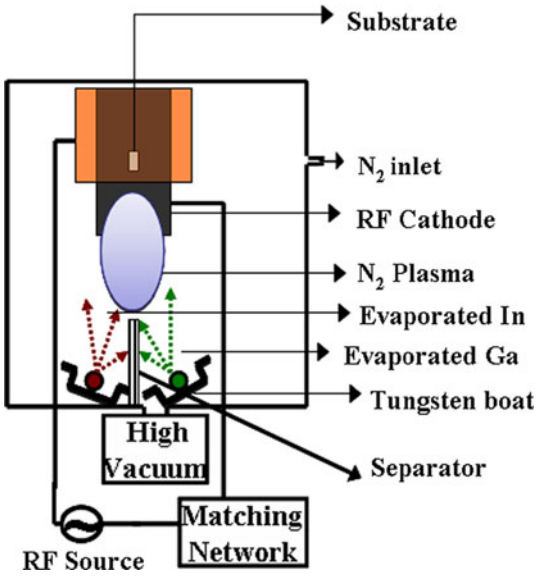

Fig. 1 Schematics of IGN thin film growth by MARE using separate sources

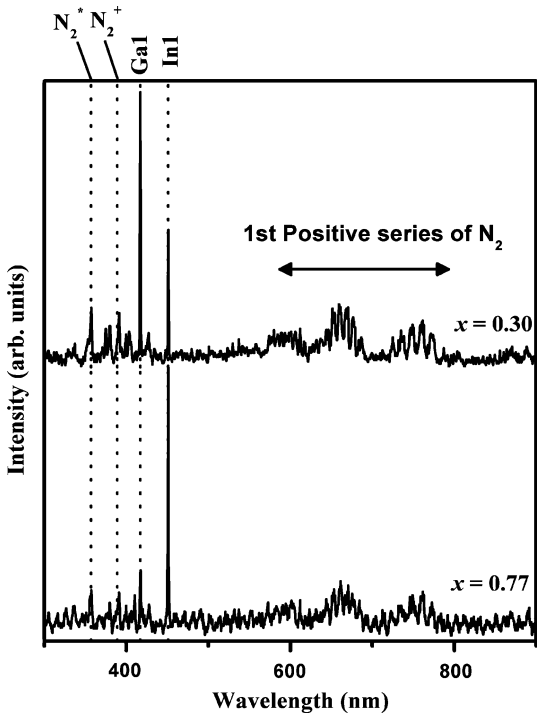

Fig. 2 Optical emission spectra for the growth of $x = 0.77$ and 0.30 IGN films

field-emission scanning electron microscope (FE-SEM) FEI Quanta 200. The surface morphology and roughness of the films are studied using Digital Instruments Nanoscope IV atomic force microscope (AFM) in contact mode. The transmittance spectra in the wavelength range (300–2000 nm) are recorded using a Jasco V-570 UV–vis-NIR spectrophotometer. The room temperature photoluminescence (PL) spectra

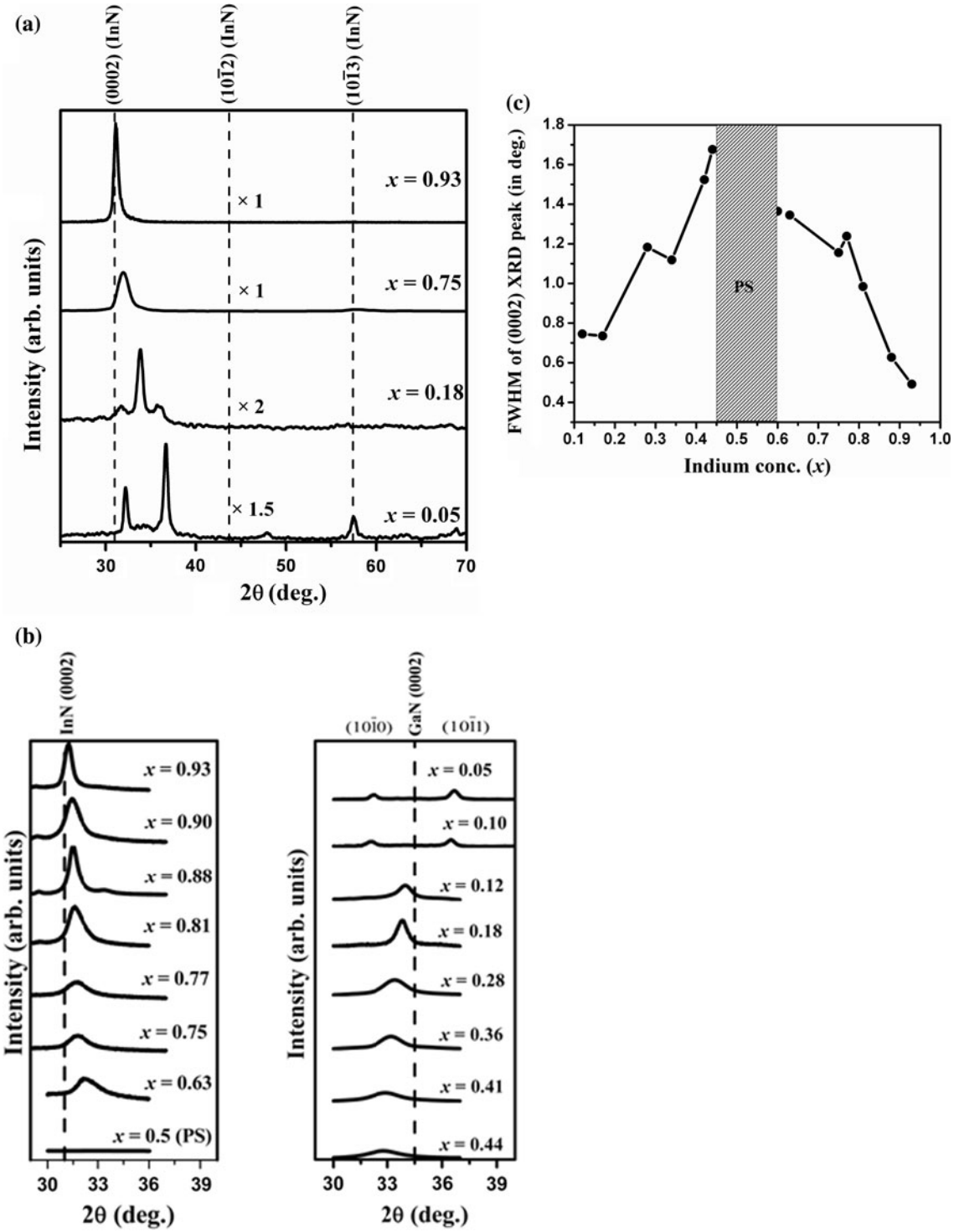

Fig. 3 **a** Full range XRD patterns of representative IGN films, **b** slow scan XRD patterns of IGN films near (0002) reflection, **c** FWHM of (0002) XRD peak as a function of indium concentration

for indium-rich IGN films are obtained using 488 nm Ar^+ laser excitation source whereas a He–Cd laser with excitation wavelength of 325 nm is used for gallium-rich films. The resistivity, carrier concentration and mobility of IGN films are measured in the van der Pauw geometry using a Lake Shore (7600 series) Hall effect system.

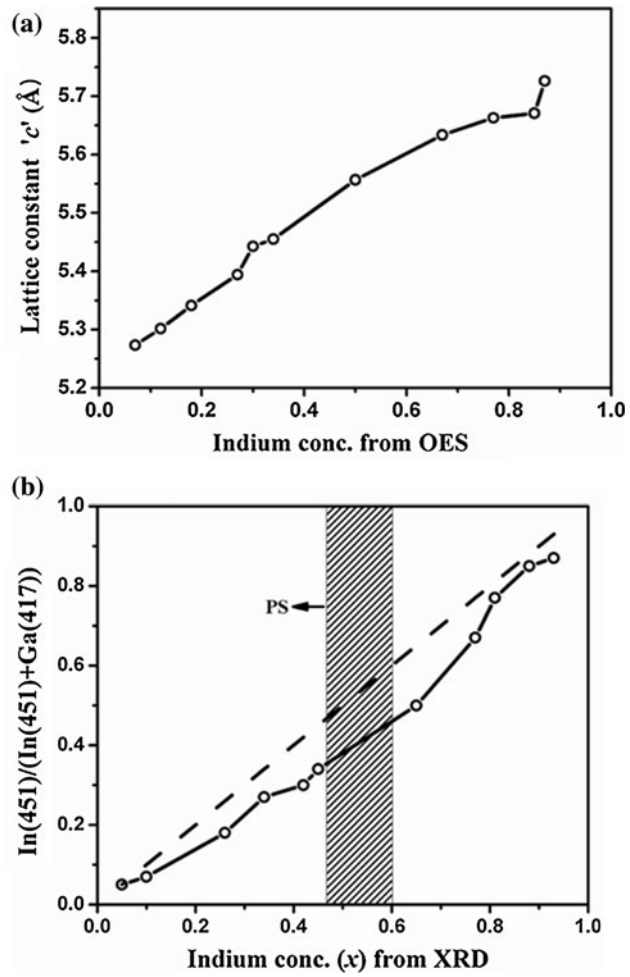

Fig. 4 **a** *c*-axis lattice parameter as a function of indium concentration obtained from OES (*solid line* is a guideline to the eye), **b** plot of indium concentration obtained from XRD as a function of excited indium species present in the plasma (*solid line* drawn is a guide to the eye and *dashed line* is a guide for ideal case)

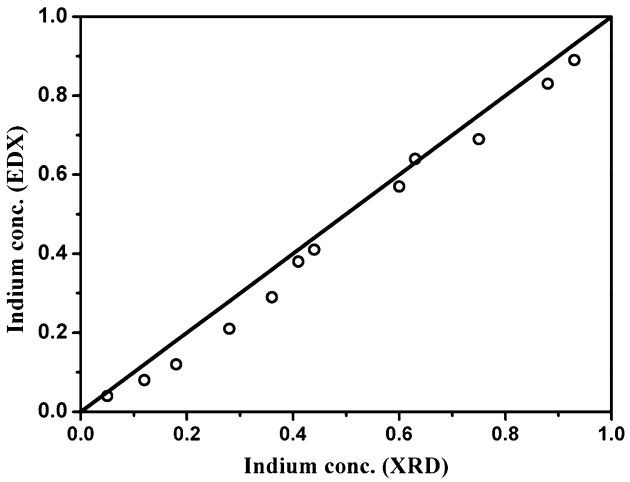

Fig. 5 Indium concentration obtained from EDX as a function of indium concentration calculated from XRD (*solid line* drawn is a guide for ideal case)

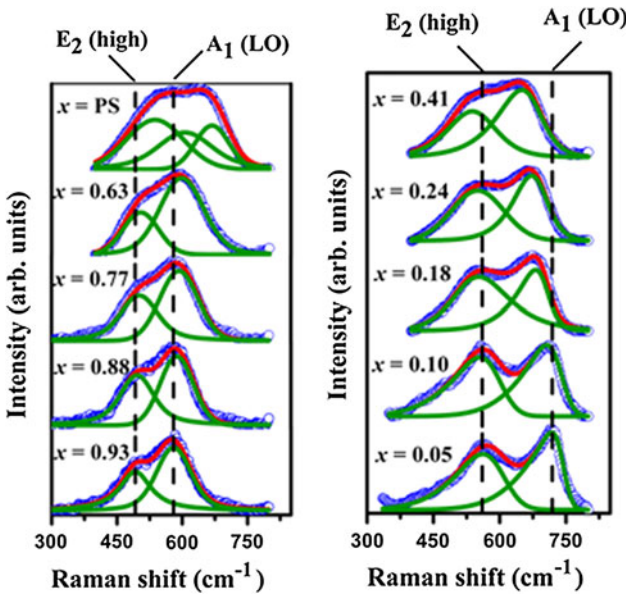

Fig. 6 Raman spectra of IGN films prepared by MARE ($\lambda_{ex} = 488$ nm)

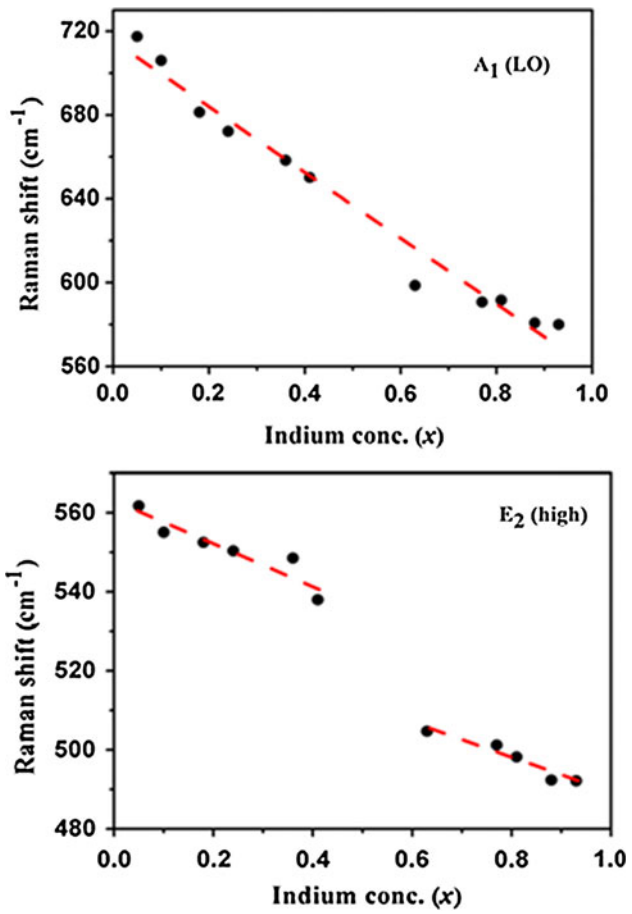

Fig. 7 A_1 (LO) and E_2 (high) peak positions as a function of indium compositions

Results and discussion

The representative XRD patterns for IGN films are plotted in Fig. 3a. All the films are found to crystallize in the hexagonal wurtzite structure with preferential growth along the *c*-axis. Weak shoulder peaks corresponding to $(10\,\bar{1}\,0)$ and $(10\,\bar{1}\,1)$ reflections are observed with increase in gallium concentration and are found to be dominating for gallium-rich films ($x < 0.10$). For some of the films, $(10\,\bar{1}\,2)$ and $(10\,\bar{1}\,3)$ reflections are also observed. For more clarity, the slow scans of XRD patterns for all the IGN films near the (0002) Bragg reflections are shown in Fig. 3b. In general, crystallites are expected to grow in all the directions. The (0002) plane in wurtzite system possesses the lowest surface energy [26]. Grains with lower surface energy become larger as the films grow and the growth develops along one crystallographic direction. For pure GaN, at lower power, it is observed that the crystallites are oriented in all the directions. In order to obtain preferential growth along the *c*-axis for pure GaN films grown by MARE technique, the films are to be grown initially at higher powers ($\sim$300 W) for 1–2 min. Since for the growth of IGN films the power is kept constant at 150 W throughout the deposition for maintaining the In/Ga ratio, the gallium-rich films could not be preferentially grown along the *c*-axis. When the IGN films with $x = 0.5$ is tried out by controlling the corresponding indium and gallium evaporation rates, a phase-segregated (PS) IGN film with a broad hump in the XRD pattern is seen. Again, the XRD peak height is an estimate of the degree of crystallinity. The crystallinity is found to be degraded for the intermediate compositions, which is mainly due to the insolubility of the alloy constituents. The onset of other crystal orientations leads to a decrease in the height of (0002) XRD peak for gallium-rich films. Further, the asymmetry of the XRD peak for indium-rich IGN films signifies the compressive strain present in them. Though comparatively less asymmetry in XRD peak is observed in Ga-rich films, they show small tensile strain. The XRD peak broadening is mainly attributed to the variations in the compositions, size effect and presence of inhomogeneous strain. Since MARE is a room temperature growth technique and the films are grown on amorphous (BSG) substrates, strain is bound to be present in these films. The

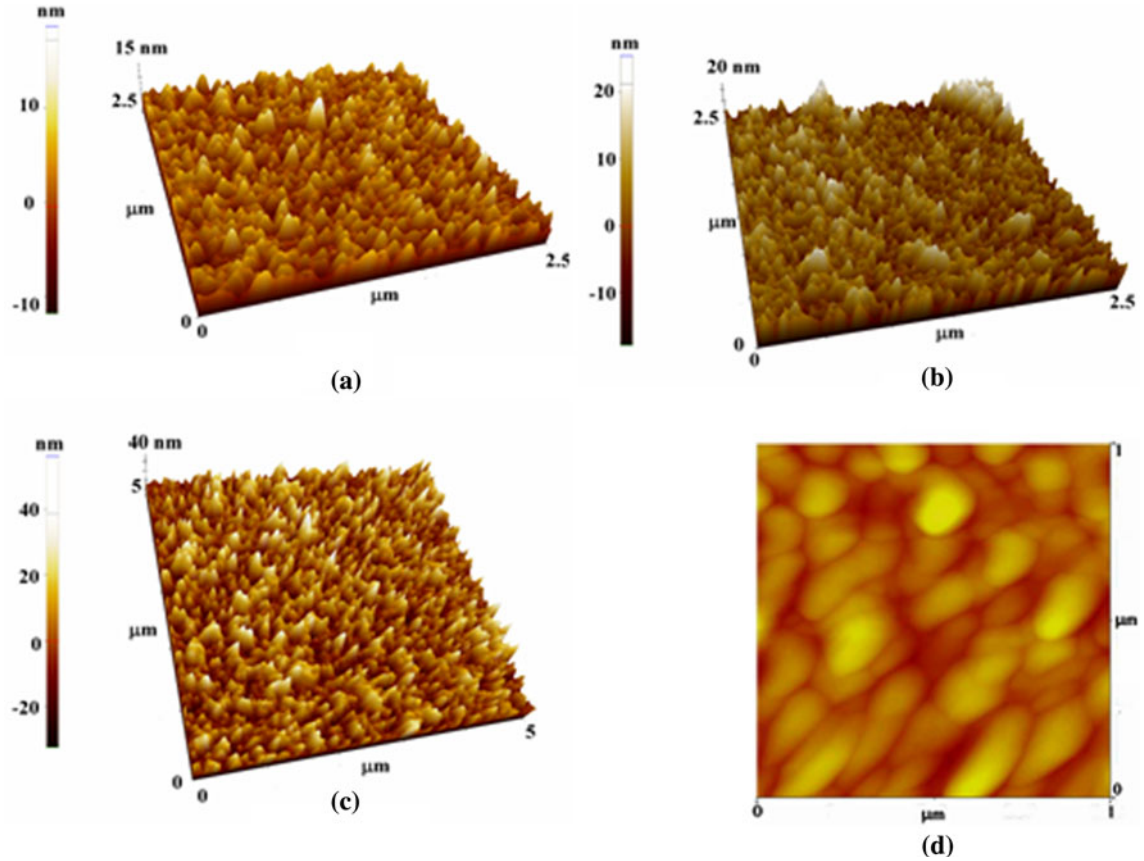

Fig. 8 AFM images of **a** $x = 0.75$, **b** $x =$ PS, and **c** $x = 0.18$ IGN films. **d** 2-dimensional AFM image for $x = 0.18$ film showing the glancing angle deposition

FWHM values for (0002) peak for different IGN films are plotted as a function of indium concentration in Fig. 3c. The FWHM reaches a maximum value for the intermediate alloy composition which is mainly due to the large amount of strain associated with the films in this region.

The indium compositions are calculated from the (0002) XRD peak shift (and $(10\bar{1}0)$ peak shift for gallium-rich films) by Vegard's law under full relaxation approximation. The variation of the *c*-axis lattice parameter as a function of excited In/Ga ratio present in the plasma is shown in Fig. 4a. The strong lines at 451.1 nm for indium and 417 nm for gallium are used to obtain the excited In/Ga ratio. The indium concentration for different IGN films obtained from XRD is found to vary from 5 to 93 %. The indium concentrations calculated from XRD peak shifts are plotted as a function of excited In/Ga ratio obtained from OES (Fig. 4b). Indium concentrations obtained from XRD peak shift by Vegard's law is overestimated under full relaxation approximation [27]. This observation is verified from the downshift of the plot shown. This downshift is pronounced near the PS region marked as a shadow in the graph; it might be due to larger overestimation of indium concentration near PS due to larger strain. In the rest of the regions, the straight line behaviour of the plot signifies the fact that the ratio of indium to gallium concentration is maintained in the resultant IGN films. Hence, OES can be considered as a powerful tool to control the stoichiometry of the films.

According to the theoretical calculations shown by Ho et al. [12], the solubility limit of InN in GaN is less than 2 % at 450 °C. But, for IGN alloy thin films, there are several reports of enhanced solubility [28] which is largely dependent on the growth technique. The phase segregation in these alloy films is mainly suppressed because of the time required for the growth of the films. Further, the presence of strain in the alloy thin films increases the solubility limit. However, XRD studies reveal that in case of MARE-grown IGN films, solubility is present in the entire alloy composition except the range $0.44 < x < 0.60$. But, compositional fluctuations leading to peak broadening are observed in all the films [25].

The In/Ga ratio is also obtained from the EDX measurement. The indium compositions obtained from EDX

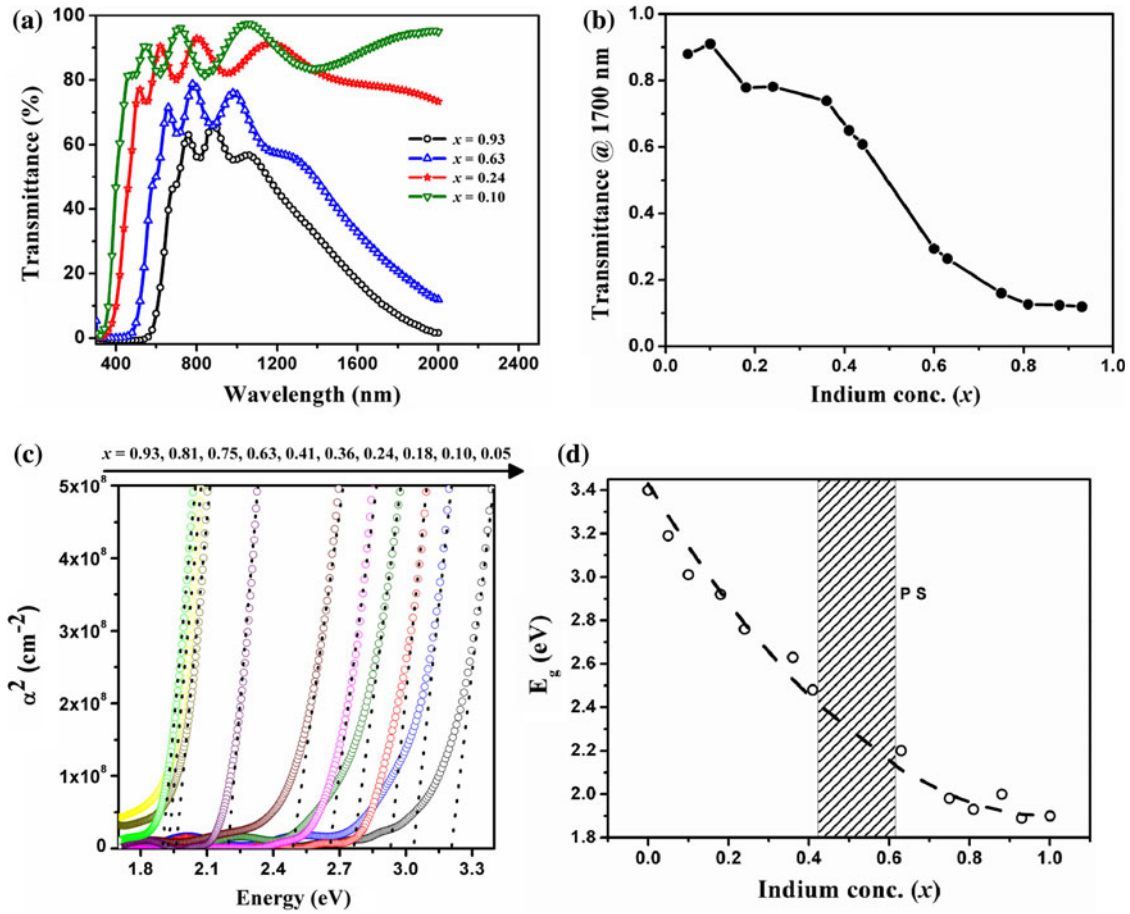

Fig. 9 **a** Transmittance spectra of IGN films prepared by MARE. **b** IR transmittance at 1700 nm as a function of indium composition. **c** Squared absorption coefficient plots for IGN films of different indium compositions. **d** Band gap variation of IGN films with indium composition (*dashed line* shows the fitting by taking the bowing parameter into account)

are lower than the values calculated from the XRD peak shift (Fig. 5). This is because indium concentration is consistently overestimated while calculating the same from XRD peak shift considering the films to be fully relaxed.

Raman spectra of IGN films excited at 488 nm for the entire composition range are shown in Fig. 6. The peaks are deconvoluted by means of Voigt lineshapes after background subtraction. All the films exhibit the characteristic A_1 (LO) and E_2 (high) modes corresponding to the hexagonal wurtzite structure. The broadening of the Raman peaks is mainly attributed to the high carrier concentrations present in the films leading to structural defects which in turn result in disorder-activated Raman scattering. The Raman peak broadening is also due to the relaxation in momentum conservation due to decrease in crystallite size. In the present case, alloy disorder and compositional fluctuations also play a significant role in the Raman peak broadening. The positions of the A_1 (LO) and E_2 (high) modes as a function of the indium composition are plotted in Fig. 7. In a ternary semiconductor $A_xB_{1-x}C$, the optical phonons may exhibit one-mode or two-mode behaviour. One mode alloys only present one set of LO and TO phonons with frequencies which show an almost linear dependence from one end member (AC) to other (BC). Two-mode behaviour alloys exhibit two sets of LO and TO phonons, the frequencies of which vary continuously from those of one end-member binary (AC, BC) to the impurity mode in the other end-member binary (BC:A and AC:B), respectively. In the present study for IGN ternary alloy, we can observe linear behaviour for the A_1 (LO) mode peak position with indium concentration. On the other hand, E_2 (high) peak positions show non-linear dependence with the composition x. It implies that A_1 (LO) mode exhibits one-mode behaviour, whereas E_2 (high) mode exhibits two-mode behaviour. These results are in agreement with the observations made by Hernandez et al. [29] and Alexson et al. [30].

The AFM images of $x = 0.75$, PS and 0.18 IGN films are shown in Fig. 8. All the films are found to be smooth with an RMS roughness of $\sim$6–7 nm. Clear grain growth is observed for $x = 0.75$ and 0.18 films, whereas the grains are found to be distorted for the phase segregated IGN film. No indium or gallium metallic clusters are observed for any of the films. The two dimensional image for $x = 0.18$ IGN films shows the elongated grains which is due to the glancing angle geometry involved during the co-evaporation process. The average grain size obtained for $x = 0.75$ and 0.18 IGN films is found to be 88 and 96 nm, respectively.

The transmittance spectra in the wavelength range 300–2000 nm for IGN films prepared by MARE technique employing separate sources are shown in Fig. 9a. The absorption edge shifts towards higher energies with increase in gallium incorporation into the lattice. This is also an indication that gallium replaces the indium atoms and vice versa in the hexagonal lattice. The NIR transmittance values at 1700 nm are plotted as a function of indium concentration in Fig. 9b. NIR transmittance is found to increase with increase in gallium incorporation which is because free carrier absorption decreases with decrease in the number of free carriers. The gallium-rich films are found to be $\sim$70 % transparent in the visible region. From the transmittance and reflectance data, the absorption coefficients and band gap values are calculated by the following relations.

$$\alpha = 2.303 \frac{\log_{10}((1-R)^2/T)}{d} \quad (1)$$

$$\alpha = A(h\nu - E_g)^{1/2} \quad (2)$$

Here, α is the absorption coefficient, T is the transmittance, R is the reflectance, d is the film thickness, E_g is the direct band gap and A is a constant. The energy band gap values can be determined by plotting the squared absorption coefficient (α^2) as a function of photon energy ($h\nu$) and linearly extrapolating it to $\alpha = 0$ (Fig. 9c).

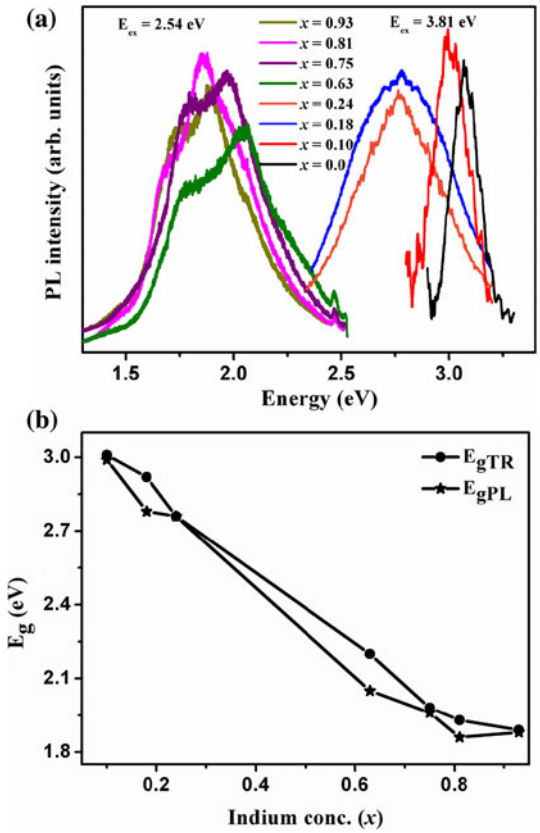

Fig. 10 **a** Room temperature PL spectra for IGN films grown by MARE. **b** Comparison of the band gap values obtained from PL measurements and transmittance measurements

The band gap values obtained from the $\alpha^2 \sim$ hv plots are plotted as a function of the indium concentration in Fig. 9d. The data are fitted with the following equation [31]:

$$F(x) = P_1(1-x) + P_2(x) - Bx(1-x) \quad (3)$$

where, $F(x)$ is the energy gap as a function of composition x. P_1 and P_2 represent the band gap at $x = 0$ and $x = 1$, respectively, and B is the bowing parameter. The fitted parameters are given as $P_1 = 3.43$ eV (E_g for GaN), $P_2 = 1.90$ eV (E_g for InN) and $B = 1.52$ eV. The band gap values obtained for pure InN and GaN match well with those obtained experimentally. The small bowing parameter matches well with the recent literature values [31]. The lowering of band gap values for indium-rich films can be attributed to the compensation of Burstein–Moss (B–M) shift due to gallium incorporation into the lattice.

The room temperature PL spectra for IGN films are shown in Fig. 10a. For indium-rich films, 488-nm excitation is used, whereas 325-nm excitation is used for the gallium-rich films. The PL peaks for indium-rich samples are broader as compared to those of gallium-rich ones. This is mainly due to higher density of structural defects present in indium-rich samples. The band gaps obtained from absorption spectra ($E_{g\mathrm{TR}}$) follow nearly the same trend as those obtained from PL measurements ($E_{g\mathrm{PL}}$) (Fig. 10b). The slight difference between $E_{g\mathrm{TR}}$ and $E_{g\mathrm{PL}}$ is due to the difference in the momentum selection rule between the absorption and luminescence. The optical absorption occurs between the states in the valance band and states above the Fermi level in the conduction band under the momentum (k) selection rule, while the luminescence represents the recombination of electrons distributed up to the Fermi level with the localized holes in the tail states without conserving k [32].

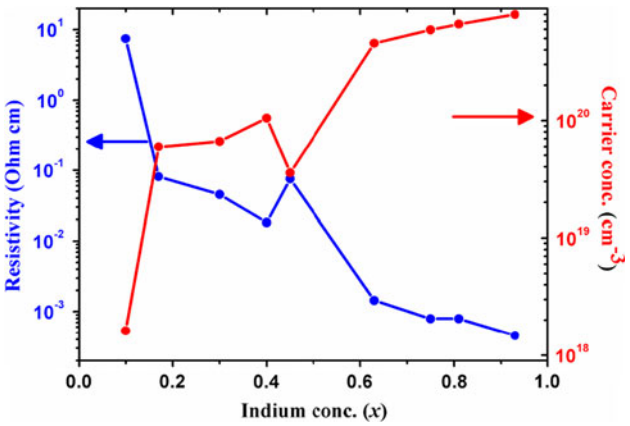

Fig. 11 Room temperature electrical resistivity and carrier concentration as a function of indium composition

The room temperature electrical resistivity and carrier concentration as a function of indium composition are shown in Fig. 11. The carrier concentration decreases by 2 orders of magnitude with increase in gallium concentration which is in accordance with the free carrier absorption observed in transmittance spectra. All the films exhibit n-type conductivity. The unintentional incorporation of impurities plays a significant role in the conductivity type in GaN and InN. In particular, hydrogen acts as a shallow donor in these semiconductors. Both interstitial and substitutional hydrogen have high solubility and give rise to n-type conductivity. From theoretical calculation, it has been proved that hydrogen acts as a double donor in group-III nitride thin films [33]. Nitrogen interstitials and nitrogen on In\Ga antisite defects can also be one of the major reasons for n-type conductivity of these IGN films [34]. The antisite defect is a double donor and with a shallow first ionization energy level and is therefore a candidate for the supply of the high background donor concentration. Together with this, unintentionally doped oxygen also contributes to the n-type conductivity in these IGN films. The room temperature mobility values of IGN films are given in Table 1. The low mobility values are mainly due to the low temperature involved in the MARE process. Low temperature introduces significant amount of structural defects in the lattice which in turn results in residue imperfection scattering and thereby lowers the mobility values. Owing to the high carrier concentration, electron–electron scattering also leads to a decrease in the carrier mobility.

The structural, optical and electrical properties of IGN films prepared by MARE technique are summarized in Table 1.

Table 1 Summary of structural, optical and electrical properties of IGN films grown by MARE

x (XRD)	x (EDX)	$E_{g\mathrm{TR}}$ (eV)	$E_{g\mathrm{PL}}$ (eV)	Resistivity (Ohm cm)	Carrier conc. (cm^{-3})	Mobility (cm^2 V s^{-1})
0.93	0.89	1.89	1.88	4.54×10^{-4}	9×10^{20}	14
0.81	0.78	1.93	1.86	7.93×10^{-4}	6.6×10^{20}	11
0.75	0.71	1.98	1.96	8.90×10^{-4}	5.2×10^{20}	13
0.63	0.64	2.2	2.05	1.44×10^{-3}	4.5×10^{20}	9
0.36	0.29	2.63	–	4.53×10^{-2}	6.6×10^{19}	2
0.24	0.21	2.76	2.76	6.24×10^{-2}	6.2×10^{19}	~1
0.18	0.12	2.92	2.78	9.1×10^{-2}	5.9×10^{19}	~1
0.10	0.08	3.01	2.99	7.48	1.6×10^{18}	~1

Conclusion

IGN films in the entire composition range are prepared on BSG substrates by separate source MARE technique. OES is used to control the In/Ga ratio in these alloy films. All the films are found to crystallize in the hexagonal wurtzite structure. From XRD, the phase segregation is observed in $0.44 < x < 0.60$ composition range. From the Raman spectroscopy measurements, the characteristic A_1 (LO) mode is found to exhibit two-mode behaviour where as E_2 (high) mode is found to follow one-mode behaviour. The band gap of IGN films could be successfully tailored from 1.88 to 3.22 eV. The band gap values obtained from optical absorption data are found to follow the same trend as obtained from PL measurements. All the films exhibited *n*-type conductivity with carrier concentration decreasing with increase in gallium incorporation. The separate source MARE turns out to be a powerful technique to grow IGN films in the entire composition range at room temperature which has got potential applications in flexible electronics. The phase segregation window for IGN films can further be narrowed down using a suitable buffer layer-like GaN and post-deposition annealing.

References

1. Nakamura S, Fasol G (1997) The blue laser diode. Springer, Berlin p 201
2. Nakamura S, Senoh M, Iwasa N, Nagahama S, Yamada T, Mukai T (1995) Jpn J Appl Phys 34:L1332
3. Yam FK, Hassan Z (2008) Superlattices Microstruct 43:1
4. Wu J, Walukiewicz W (2003) Superlattices Microstruct 34:63
5. Davydov VYu, Klochikhin AA, Seisyan RP, Emstev VV, Ivanov SV, Bechstedt F, Furthmuller J, Harima H, Mudryi AV, Aderhold J, Semchinova O, Graul J (2002) Phys Status Solidi B 229:r1
6. Mann AK, Varandani D, Mehta BR, Malhotra LK (2007) J Appl Phys 101:084304
7. Motlan, Goldys EM, Tansley TL (2002) J Cryst Growth 241:165
8. Tansley TL, Foley CP (1986) J Appl Phys 59:3241
9. Shubina TV, Ivanov SV, Jmerik VN, Solnyshkov DD, Vekshin VA, Kop'ev PS, Vasson A, Leymarie J, Kavokin A, Amano H, Shimono K, Kasic A Monemar B (2004) Phys Rev Lett 92:117407
10. Chen PPT, Butcher KSA, Fouqueta MW, Wuhrer R, Phillips MR, Prince KE, Timmers H, Shrestha SK, Usher BF (2006) J Cryst Growth 288:241
11. Butcher KSA, Tansley TL (2005) Superlattices Microstruct 38:1
12. Ho I, Stringfellow GB (1996) Appl Phys Lett 69:2701
13. Lu H, Thothathiri M, Wu Z, Bhat I (1997) J Electron Mater 26:281
14. Chaley VP, Borisov BA, Domidov DM, Karsovitsky DM, Pogorelsky YV, Shkurko AP, Sokolov IA, Karpov SY (1999) J Cryst Growth 206:147
15. Osamura KS, Murakami Y (1975) J Appl Phys 46:3432
16. Shinoda H, Mutsukura N (2008) Thin Solid Films 516:2837
17. Kobayashi A, Ohta J, Fujioka H (2006) J Appl Phys 99:123513
18. Kim S, Lee K, Lee H, Park K, Kim CS, Son SJ, Yi KW (2003) J Cryst Growth 247:55
19. Nath DN, Gur E, Ringel SA, Ranjan S (2010) Appl Phys Lett 97:071903
20. Kim HM, Lee WC, Kang TW, Chung KS, Yoon CS, Kim CK (2003) Chem Phys Lett 380:181
21. Biju KP, Subrahmanyam A, Jain MK (2008) J Phys D Appl Phys 41:155409
22. Biju KP, Jain MK (2009) J Cryst Growth 311:2275
23. Meher SR, Biju KP, Jain MK (2009) AIP Conf Proc 1147:457
24. Meher SR, Biju KP, Jain MK (2011) Appl Surf Sci 257:8623
25. Meher SR, Biju KP, Jain MK (2011) Phys Status Solidi A 208:2655
26. Yadav BS, Major SS, Srinivasa RS (2007) J Appl Phys 102: 073516
27. O'Donnell KP, Mosselmans JFW, Martin RW, Pereira S, White ME (2001) J Phys Condens Matter 13:6977
28. Singh R, Doppalapuddi D, Moustakas TD, Romano LT (1997) Appl Phys Lett 70:1089
29. Hernandez S, Cusco R, Pastor D, Artus L, O'Donnell KP, Martin RW, Watson IM, Nanishi Y, Calleja E (2005) J Appl Phys 98:013511
30. Alexson D, Bergman L, Nemanich RJ, Dutta M, Stroscio MA, Parker CA, Bedair SM, El-Marsy NA, Adar F (2001) J Appl Phys 89:798
31. Kuykendall T, Ulrich P, Aloni S, Yang P (2007) Nat Mater 6:951
32. Guo QX, Tanaka T, Nishio M, Ogawa H, Pu XD, Shen WZ (2005) Appl Phys Lett 86:231913
33. Van de Walle CG, Lyons JL, Janotti A (2010) Phys Status Solidi A 207:1024
34. Stampfl C, Van De Walle CG, Voggel D, Krugger P, Pollman J (2000) Phys Rev B 61:R7846